Journal of Energy Chemistry 72 (2022) 26–32

Contents lists available at ScienceDirect

Journal of Energy Chemistry

journal homepage: www.elsevier.com/locate/jechem

http://www.journals.elsevier.com/journal-of-energy-chemistry/

Etching-courtesy NH_4^+ pre-intercalation enables highly-efficient Li^+ storage of MXenes via the renaissance of interlayer redox

Junyan Li [a,b], Wei Zhang [a,*], Xin Ge [a], Ming Lu [b,*], Xiangxin Xue [b], Zizhun Wang [a], Nailin Yue [a], Junkai Zhang [b], Xingyou Lang [a], Qing Jiang [a], Weitao Zheng [a,*]

[a] Key Laboratory of Automobile Materials MOE, School of Materials Science & Engineering, Jilin Provincial International Cooperation Key Laboratory of High-Efficiency Clean Energy Materials, Electron Microscopy Center, and International Center of Future Science, Jilin University, Changchun 130012, Jilin, China
[b] The Joint Laboratory of MXene Materials, Key Laboratory of Functional Materials Physics and Chemistry of the Ministry of Education, Key Laboratory of Preparation and Application of Environmental Friendly Materials of the Ministry of Education, Jilin Normal University, Changchun 130103, Jilin, China

ARTICLE INFO

Article history:
Received 20 March 2022
Revised 13 April 2022
Accepted 14 April 2022
Available online 23 April 2022

Keywords:
Mo_2CT_x MXene
Ammonium ions
Intercalation
Lithium storage

ABSTRACT

Inspired by a well-known architecture notion that load-bearing walls enable maintaining a highly-stable multiple-floored building, superior advantages are afforded via fabricating the NH_4^+ ions pre-intercalated Mo_2CT_x MXene (Mo_2CT_x-N) in a mixed solution of NH_4F and HCl via a simple one-step hydrothermal method. As a result of the synergistic effects of pillared structure, immobilizing -F groups and unlocking Mo-based redox, the Mo_2CT_x-N remarkably delivered a reversible capacity of 384.6 mAh g^{-1} at 200 mA g^{-1} after 100 cycles. Our work lays a foundation for fully packaging its optimal performance via carding and architecting the chemistry of the MXene layers and between them.

1. Introduction

Safe, environment-friendly and low-cost energy storage technology has been energetically spurred on by the increasing energy crisis and environmental pollution. Lithium-ion batteries (LIBs) have been widely utilized in portable electronic devices, electric vehicles, and grid-level energy storage due to their lightweight, stable performance, non-memory effect and high energy density [1–3]. However, the calculated capacity of the conventional graphite anode (372 mAh g^{-1}) [4] cannot satisfy the updated demand for high energy and power densities of LIBs. Therefore, exploring the alternative high specific capacity anode materials has become one of the major challenges for LIBs.

Selectively etching "A" atom layers from the MAX (M: transition metal, X: carbides, nitrides or carbonitrides, A: metal) ceramic materials can gain long-range ordered MX atom arrangement, which shows 2D features and is named as "MXenes". M layers are nearly closed packed, while the carbon and/or nitrogen X atoms fill the octahedral sites [5]. M atoms provide abundant redox-active sites as well as facilitate rapid electron transport in the electric plane [6,7]. Confined by the adjacent MX layers, forming geometrically arranged subnanometer interlayers can offer rapid ion intercalation and transport [8–11]. Meanwhile, anions in the etchant connect with M atoms to form surface functional groups, such as O, OH and/or F [5,12,13]. Besides, the surface terminations of MXenes can be tailored toward certain redox chemistries [14–16]. Based on the aforementioned characteristics, MXenes with high electronic/ionic transport are becoming promising electrode materials [17–20].

It is urgent for unlocking the capacity fading of MXenes, owing to the limited ion storage capacity under a complicated chemical environment. It ranges from the limited distance of interlayers to the preparation-derived disorder and the intrinsic electrochemically unfavorable surface functional groups (e.g., F) [21,22]. For a typical Mo_2CT_x MXene offering a larger interlayer spacing and a higher theoretical capacity of 526 mAh g^{-1} [23], stack-collapsing of the interlayer structure of 2D materials upon cycles is the arch-criminal for its capacity deterioration [24,25]. Besides, owing to the intrinsic electrochemically unfavorable -F groups bonding with Mo, the redox reaction of the Mo atoms of the Mo_2CT_x is restricted. Thus, many efforts are thereof made to focus on the interlayer environment confined MXene layers. Well accepted, the interlayer spacing of MXene is expected to expand by using a range of intercalants, such as ions [26,27], organic molecules [28], nanoparticles [29], nanowires [30] and nanosheets [31,32]. To realize atomic-level modulation, ionic confinement effects

* Corresponding authors.
E-mail addresses: weizhang@jlu.edu.cn (W. Zhang), luming@jlnu.edu.cn (M. Lu), wtzheng@jlu.edu.cn (W. Zheng).

https://doi.org/10.1016/j.jechem.2022.04.030

within MXene's interlayer spacing are widely investigated. Ionic pre-intercalated engineering designed interlayer environment of MXene enables being precisely matched with the requirement of ion intercalated electrodes toward the improvement of electrochemical performance [15].

The popular architecture and design principle lie that a wholly-stable and floors-tidy office building enables peacefully accommodating more staff and stuff. Inspired by the load-bearing wall (LBW) that maintains the stability of the building, we propose that through NH_4^+ ions pre-intercalated Mo_2CT_x as the "LBW" to maintain a highly stable internally layered framework to allow for highly efficient and enhanced ionic intercalation. Herein, through a simple one-step hydrothermal method, NH_4^+ interacted Mo_2CT_x MXene was obtained using a mixed solution of NH_4F and HCl. NH_4^+ was selected for pre-intercalation due to its lower adsorption energy on MXene that results in lower NH_4^+ concentration [33], and a smaller molar mass that prevents a significant reduction of theoretical capacity due to additional ion insertion. The interaction between the chemical interlayer environment and confined NH_4^+ was clarified by integrating comprehensive spectroscopy and microscopy analysis. The derived Mo_2CT_x-N exhibited a larger interlayer distance and a lower content of -F groups. Besides, monitoring the Mo_2CT_x MXene electrodes during the charge and discharge processes, Mo is activated to participate in the reversible redox reaction by offering a variable valence. Mo_2CT_x-N with a lower -F content can allow more Mo-intermediated reversible redox reaction. As of these consequences, the Mo_2CT_x-N delivered optimal cycling stability. Through delicately modifying the chemical environment of Mo_2CT_x MXene and pinpointing the Li^+ storage mechanism, our work can be extended to a wide range of MXenes and other 2D materials for highly-efficient electrochemical energy storage.

2. Experimental

2.1. Materials

Mo_2Ga_2C powders were purchased from Jilin 11 technology Co., Ltd. Hydrofluoric acid (HF, 40%) and hydrochloric acid (HCl, 38%) were obtained from Sinopharm Chemical Reagent. Ammonium fluoride (NH_4F, 98%) was obtained from Aladdin Reagent.

2.2. Synthesis of Mo_2CT_x MXene via HF

The Mo_2CT_x was prepared via the approach of HF-etched Mo_2Ga_2C [34]. 2 g of Mo_2Ga_2C powders were slowly added to 80 mL 25% HF, and the mixture was then stirred with a magnetic Teflon stir bar at 55 °C for 160 h. The mixture was centrifuged and washed with deionized water several times until pH > 6. Then the mixture was washed with ethanol. Finally, the obtained powders were dried in a vacuum oven at room temperature for 12 h. This sample was referred to as Mo_2CT_x-H.

2.3. Synthesis of Mo_2CT_x MXene via NH_4F/HCl

The Mo_2CT_x was prepared via the etching agent of NH_4F/HCl in hydrothermal conditions [35]. Firstly, the etching agent was prepared by mixing 2 g NH_4F and 40 mL 6 M HCl in an ultrasonic process for 30 min. The Mo_2Ga_2C (2 g) was immersed into the etching agent and stirred for 30 min. The mixture was transferred to 100 mL Teflon-lined stainless-steel autoclaves. The autoclaves were maintained at different temperatures (140, 160 or 180 °C) for 24 h. The process of wash samples was similar to the Mo_2CT_x-H. The Mo_2CT_x prepared via NH_4F/HCl etching at 180 °C was referred to as Mo_2CT_x-N.

2.4. Microstructural characterization

The morphologies of MXene powders were examined by using a scanning electron microscope (SEM, JSM-7900F and FEI Nova Nano 450), equipped with energy dispersive X-ray spectroscopy (EDS). The X-ray diffraction pattern (XRD) patterns of the samples were taken with a Rigaku D/max-2500 X-ray diffractometer and Rigaku D/max-2600 X-ray diffractometer under Cu $K\alpha$ radiation (λ = 0.15 406 nm). Transmission electron microscopy (TEM, JEM-2100F) was used to obtain the high-resolution TEM (HRTEM) images. Scanning transmission electron microscopy (STEM) and electron energy loss spectroscopy (EELS) were examined by using JEM ARM 300F GRAND ARM. X-ray absorption spectra (XAS) of Mo K-edge were collected in the range of 19.83–20.616 keV at Shanghai Synchrotron Facility (SSRF) on beamline BL14. Soft X-ray absorption spectroscopy (SXAS) of N K-edge was collected in the range of 385–425 eV at Singapore Synchrotron Light Source (SSLS) on beamline XAFCA. X-ray photoelectron spectroscopy (XPS) measurements were conducted on Thermo Scientific Escalab 250XI. Raman spectra were estimated using a Via Raman spectrometer (WITec alpha300 R, 532 nm), conducted by the TESCAN RISE (S9000G). Fourier transform infrared (FTIR) spectroscopy was carried out on a Nicolet iS10 Therom Fisher Scientific spectrophotometer using KBr pellets.

2.5. Electrochemical measurements

The electrochemical behavior was investigated using half coin cells (CR 2032). The working electrodes were prepared by mixing as-active Mo_2CT_x-H or Mo_2CT_x-N MXene powders with Super P and polyvinylidene fluoride (PVDF) with a weight ratio of 6:2:2 banded in N-methyl-2-pyrrolidinone (NMP), and the resulting slurry was coated on copper foils. The copper foils were moved into a vacuum oven and maintained at 70 °C for 12 h. The coin cells were assembled in an argon-filled glove box with concentrations of moisture and oxygen below 0.5 ppm. Li sheets were used as the counter and reference electrodes, and 20 μm microporous trilayer membranes (Guangdong Candle New Energy Technology Co., Ltd.) were used as separators. 1 M $LiPF_6$ solution in ethylene carbonate/diethyl carbonate/ethyl methyl carbonate (EC/DEC/EMC) (1:1:1 in volume) was used as the electrolyte (40 μL used in the cell). The electrochemical workstations (Chenhua CHI660e, and Metrohm Autolab PGSTAT302N) and the battery test system (CT-4008 T, NEWARE) were employed to evaluate the performance of lithium storage.

3. Results and discussion

The synthesis of Mo_2CT_x MXene is schematically illustrated in Fig. 1(a). In the first method, the Mo_2Ga_2C powders were etched at 55 °C via the magnetic stirring method in 25% HF for 160 h. For the second, Mo_2Ga_2C powders were etched via the hydrothermal method in the mixed solution of NH_4F and HCl at 140, 160 and 180 °C for 24 h, respectively. Pure Mo_2CT_x was obtained until the temperature increased up to 180 °C. (Fig. S1).

3.1. Structural characterization

As shown in Fig. 1(b and c), the XRD patterns exhibit that these peaks positionally assigned to Mo_2Ga_2C are almost replaced by the peaks of Mo_2CT_x. As a typical feature of MAX to MXene, the (002) peak of Mo_2Ga_2C MAX at 9.87° shifts left to 9.21° (Mo_2CT_x-H) or 8.47° (Mo_2CT_x-N). The corresponding interlayer distances were calculated, via Bragg's equation, as 8.95 Å (Mo_2Ga_2C), 9.59 Å (Mo_2CT_x-H) and 10.39 Å (Mo_2CT_x-N). It is worth noting that the interlayer

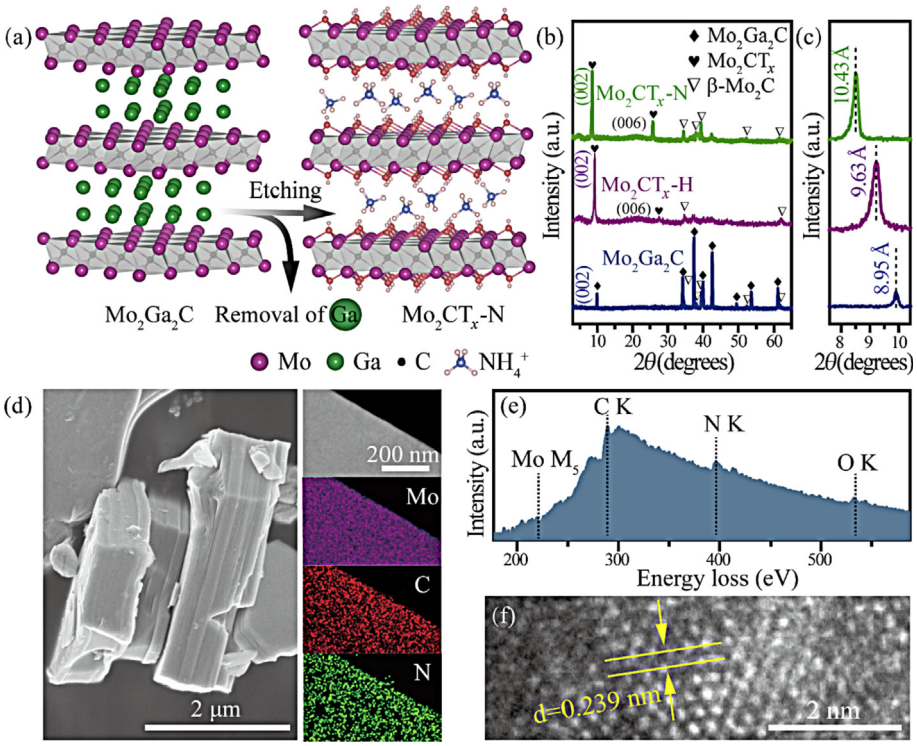

Fig. 1. Fabrication and characterization of Mo_2CT_x-N. (a) Schematic of the Mo_2CT_x-N synthesis. (b) Full range XRD patterns of Mo_2Ga_2C, Mo_2CT_x-H and Mo_2CT_x-N, and (c) the enlarged (002) peaks. (d) SEM, STEM images and the corresponding EDS elemental maps, (e) EELS and (f) HRTEM image of Mo_2CT_x-N.

distance of Mo_2CT_x-N is larger than that of Mo_2CT_x-H, attributed to the cations intercalated into MXene and pillared the interlayers [36]. Moreover, the full width at half maximum (FWHM) of Mo_2CT_x-N (0.22°) is smaller than that of Mo_2CT_x-H (0.37°) (Table S1), indicating an increased order degree of Mo_2CT_x-N owing to the electrostatic attraction [37] between the NH_4^+ and electronegative Mo_2CT_x.

SEM images are shown in Fig. 1(d) and Fig. S2(a-f). The Mo_2CT_x-H and Mo_2CT_x-N sheets appear rather than the accordion-like morphology of $Ti_3C_2T_x$. Besides, the average sizes of Mo_2CT_x-N and Mo_2CT_x-H nanoparticles were counted by using the SEM images (Fig. S3) and listed in Table S2. They are quite similar, indicating that NH_4^+ ions intercalation has no obvious effect on the size of Mo_2CT_x particles. The EDS elemental mapping (Fig. S2 and S4) demonstrates an obvious reduction of Ga after etching and less F of Mo_2CT_x-N.

STEM images and EDS elemental maps of Mo_2CT_x-N are also presented in Fig. 1(d). The uniform distribution of N element was detected across the Mo_2CT_x-N due to NH_4^+ within the layers or on the surface of Mo_2CT_x-N. Besides, EELS (Fig. 1e) confirms the existence of N element. As measured by the HRTEM images (Fig. S5 and Fig. 1f) from the edge of the Mo_2CT_x-H and Mo_2CT_x-N sheets, (103) plane is well identified [38]. Besides, HRTEM images of Mo_2CT_x-N (Fig. S6) show the 2D multilayer structure of MXene.

In order to explore the possible change for Mo atoms of Mo_2CT_x-H and Mo_2CT_x-N, X-ray absorption near edge structure spectroscopy (XANES) was performed for Mo K-edge. The K-edge of Mo of Mo_2CT_x-N shifts to lower energy (Fig. 2a) that is consistent with a decrease in the average oxidation state [39] of the metal atoms. Moreover, Fourier transforms (FT) for the EXAFS are also presented in Fig. 2(b). The peaks at ~ 1.96, 2.94 and 3.8 Å are attributed to the Mo_1-C_1, Mo_1-Mo_2 and Mo_1-C_2 bonds along the *c*-axis. Compared with Mo_2CT_x-H, the three peaks for Mo_2CT_x-N shifts slightly to the lower *R* value, followed by an obviously increased intensity, indicative of shrinkage in the atomic distance and the significantly increased order degree. The obvious decrease of Mo_1-C_1, Mo_1-Mo_2 and Mo_1-C_2 bond length for Mo_2CT_x-N arises from the compressive strain along the *ab* plane (Fig. S7) [40]. This is due to the occurrence, that the NH_4^+ ions intercalated into MXene and pillared the interlayer, which is consistent with our XRD results.

SXAS spectra of Mo_2CT_x-N (Fig. S8) was fitted using partial peaks, since the excitation energy of Mo M3-edge and N K-edge are adjacent. Fig. 2(c) shows the SXAS (Molybdenum exclusion) measured at the N K-edge of Mo_2CT_x-N and NH_4F. Our SXAS of Mo_2CT_x-N and NH_4F exhibit a main band (~406 eV) and a tail due to post-edge transitions. For NH_4^+ in perfect tetrahedral symmetry, the minimum unoccupied molecular orbital (MUMO) has a_1 symmetry (i.e., pure 2*s* character without additional 2*p* contribution). As a consequence, the 1 *s*-to-MUMO transition is dipole forbidden. The main-edge peak corresponds to the transition to MUMO + 1. The MUMO + 1 in NH_4^+ has an exclusive 2*p* character, explaining the strong main-edge peaks. Besides, the main-edge peak of Mo_2CT_x-N has considerable asymmetry toward higher energies, which is due to the interaction of NH_4^+ with interlayer water or surface functional groups [41].

The functional groups of the Mo_2Ga_2C, Mo_2CT_x-H and Mo_2CT_x-N were analyzed by FTIR spectra (Fig. 2d). For all the samples, the –OH (~3670, 2990 and 2900 cm^{-1}), O–H (~1395 cm^{-1}) and C-O (~1250 and 1066 cm^{-1}) functional groups existed [42]. The peak ~ 1622 cm^{-1} of Mo_2CT_x-H can be attributed to the C = O functional group. This may result from the solvents used in the separation and drying processes and/or the exposure of the high-surface-area material at the ambient condition [43]. The peaks around 738 cm^{-1} of Mo_2CT_x-H and Mo_2CT_x-N can be assigned to the Mo-O functional group [44].

The variations of chemical compositions and element valence states were further characterized by using XPS. Compared with the Mo_2Ga_2C precursor, the Ga-related peaks of Mo_2CT_x-H and Mo_2CT_x-N disappear (Fig S9a and b), confirming that both HF and

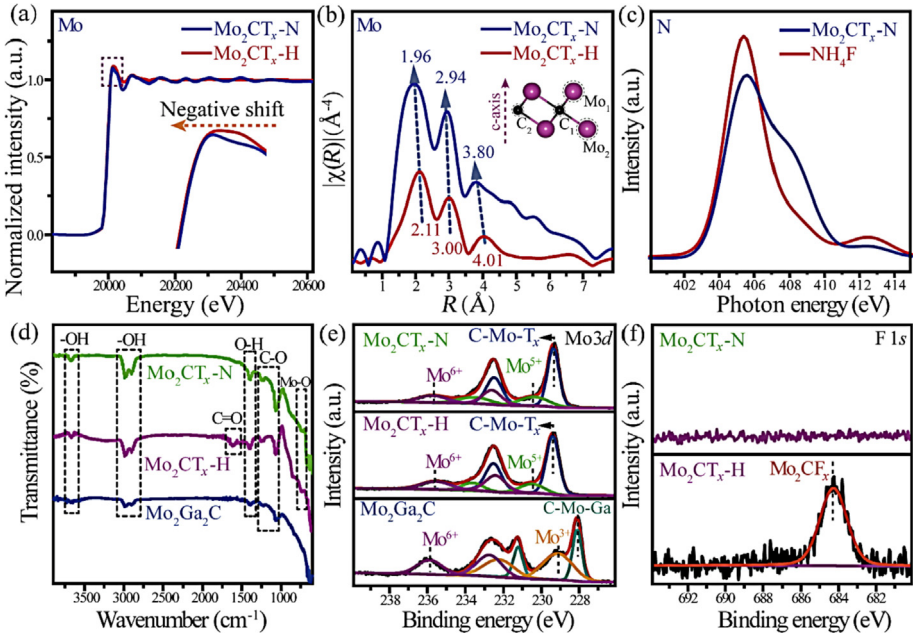

Fig. 2. Spectroscopy characterization of Mo_2CT_x-N. (a) Normalized XANES spectra, (b) Fourier transforms (FT) of EXAFS spectra of Mo_2CT_x-H and Mo_2CT_x-N. (c) N K-edge SXAS spectra of Mo_2CT_x-N (Molybdenum exclusion) and NH_4F. (d) FTIR spectra, and (e) Mo 3*d* spectra of Mo_2Ga_2C, Mo_2CT_x-H and Mo_2CT_x-N. (f) High-resolution F 1*s* spectra of Mo_2CT_x-H and Mo_2CT_x-N.

NH_4F/HCl routes can effectively remove the Ga layers. The high-resolution spectra for Mo 3*d* are shown in Fig. 2(e). The high-resolution spectrum of the Mo 3*d* region for Mo_2Ga_2C was divided into three pairs of peaks of C-Mo-Ga, Mo^{3+} and Mo^{6+} [45,46]. The Mo 3*d* region for Mo_2CT_x-H and Mo_2CT_x-N were fitted by the following three species: C-Mo-T_x, Mo^{5+}, and Mo^{6+} [46,47]. The binding energy (BE) of the C-Mo-T_x species is higher than the C-Mo-Ga species, which is due to the replacement of some elements with more electronegative surface terminations, such as -O, –OH and -F [48]. Because the binding energy of F^- and NH_4^+ is higher than Mo_2CF_x, F^- is more likely to combine NH_4^+ to form NH_4F. The -F content of Mo_2CT_x-N is lower than that of Mo_2CT_x-H (Fig. 2f). As a result, it tends to faster ion transport and more active sites exposed to the electrolyte [22]. Besides, the XPS survey spectra, high-resolution O 1 *s* and C 1 *s* are shown in Fig. S9. The XPS O 1 *s* peaks of Mo_2CT_x-H and Mo_2CT_x-N (Fig. S9c) were assigned to the following species: Mo_2CO_x (-O terminated) and $Mo_2C(OH)_x$ (–OH terminated). The structure was analyzed by Raman spectra (Fig. S10).

3.2. Electrochemical performance

Electrochemical performance comparisons were conducted between Mo_2CT_x-H and Mo_2CT_x-N. The typical cyclic voltammetry (CV) curves (the 5th cycle) are shown in Fig. 3(a). The reversible redox peaks of Mo_2CT_x-H (1.39/0.56 V) and the Mo_2CT_x-N (1.14/1.02 V) are ascribed to Li^+ deintercalation from/intercalation into the Mo_2CT_x. Other anodic peaks of Mo_2CT_x-H (2.36 V) and Mo_2CT_x-N (2.19 V) are attributed to phase transformations between various oxides upon cycling (monoclinic and orthorhombic phases) [47]. In addition, the integrated areas of the 5th CV curves (Fig. 3a) reveal that the initial capacitance of Mo_2CT_x-N is lower than Mo_2CT_x-H. The CV curves for the first 5 cycles (Fig. S11a and b) and at different scan rates (Fig. S11c and d) reveal the initial irreversible reaction and the polarization effects [49].

To explain the electrochemical performance, the kinetics of the Mo_2CT_x-N electrodes for Li^+ storage was analyzed by testing the CV curves at various scan rates (Fig. S11c and d). Fig. S11(e) presents the dependence of log(*i*) versus log(*v*) for the redox peaks of Mo_2CT_x-N electrode in CV curves (*i* refers to the peak current density, and *v* is the scan rate). According to $i=av^b$, the fitting slope (*b*-value) of the plots is well established as an indicator for the electrochemical kinetics. The *b*-value of 1 represents a complete capacitive-controlled behavior through a surface faradaic redox reaction and the *b*-value of 0.5 indicates a diffusion-controlled process resulting from electrolyte ions intercalation and transport [27]. The *b*-value of peaks O_1 and O_2 is close to 0.5, which implies that the operating mechanism is controlled by diffusion.

According to the classical Randles Sevcik equation, the Li^+ diffusion can be estimated as follows,

$$I_p = \left(2.65 \times 10^5\right) n^{1.5} S D_{Li+}^{0.5} \Delta C_{Li} v^{0.5}$$

where, I_p is peak current, *n* is the number of electrons, *S* is the active electrode area, D_{Li+} is the Li^+ diffusion coefficient, ΔC_{Li} is the Li^+ concentration change in the electrochemical reaction, and *v* is the scanning rate. The slopes of the curves ($I_p/v^{0.5}$) (Fig. S11f) should positively correlate to the D_{Li+} in each step of the sulfur redox reaction, since the values of *n*, *S*, and ΔC_{Li} are constant. Obviously, the slope of the Mo_2CT_x-H is higher than that of Mo_2CT_x-N, suggesting the faster Li^+ diffusion rate of Mo_2CT_x-H [50]. This may be attributed to the cations confined by the adjacent MXene layers, probably leading to an electrostatic repulsion effect on the lithiation [51].

The galvanostatic charge–discharge (GCD) profiles (Fig. 3b and S12) show the charge/discharge plateaus, which are consistent with the redox peaks in CV curves. The GCD curves are oblique lines with no charging and discharging platform at the initial stage. This is possible because the charge/discharge of Mo_2CT_x is dominated by the capacitive process at the corresponding voltage [52]. Meanwhile, GCD curves of Mo_2CT_x-H and Mo_2CT_x-N electrodes at different current densities (Fig. S12c and d) show the absence of the charge/discharge plateaus with the increase of current densities, indicating the diffusion capacity reduced with the increase of current densities.

To illustrate the characteristics of electron and ion transfer, electrochemical impedance spectroscopy (EIS) tests were conducted in a frequency ranging from 100 kHz to 100 mHz (Fig. 3c). The equivalent series resistance (R_s) of Mo_2CT_x-H and

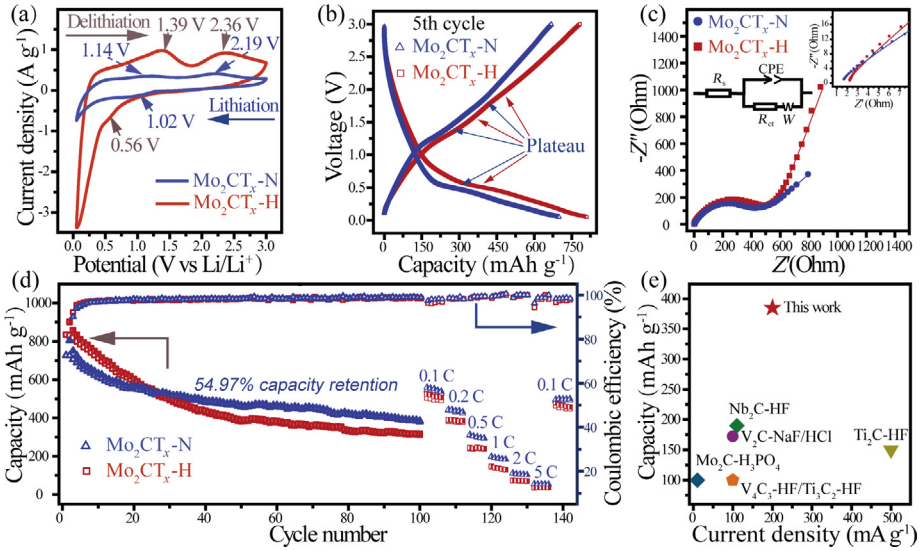

Fig. 3. Electrochemical characterization of Mo_2CT_x. (a) CV curves of Mo_2CT_x-H and Mo_2CT_x-N electrodes at 1 mV s^{-1} for the 5th cycle. (b) Galvanostatic charge/discharge curves of the 5th cycle. (c) EIS spectra, the inset shows the magnified high-frequency region. (d) Cycling stability at a current density of 200 mA g^{-1} and rate capabilities. (e) Gravimetric capacity of Mo_2CT_x-N with a series of reported MXenes for LIBs.

Mo_2CT_x-N are 1.769 and 1.046 Ω, respectively, which were calculated via the *x*-intercept of the Nyquist plot. The lower R_s of Mo_2CT_x-N electrode shows a lower electrode resistance [53]. The diameter of the semicircle arc is related to the charge-transfer resistance (R_{ct}) [54–56]. The R_{ct} value of the Mo_2CT_x-N electrode is much lower (Table S3), indicating the excellent conductivity of Mo_2CT_x-N. The Mo_2CT_x-N electrode shows a smaller slope in the low-frequency region, indicating the lower ions transfer kinetics [57] of Mo_2CT_x-N, which is consistent with our CV results.

Fig. 3(d) shows the galvanostatic charge/discharge curves of Mo_2CT_x-H and Mo_2CT_x-N anode. The Mo_2CT_x-N delivered a lower capacity in the initial 27 cycles. This may be attributed to the

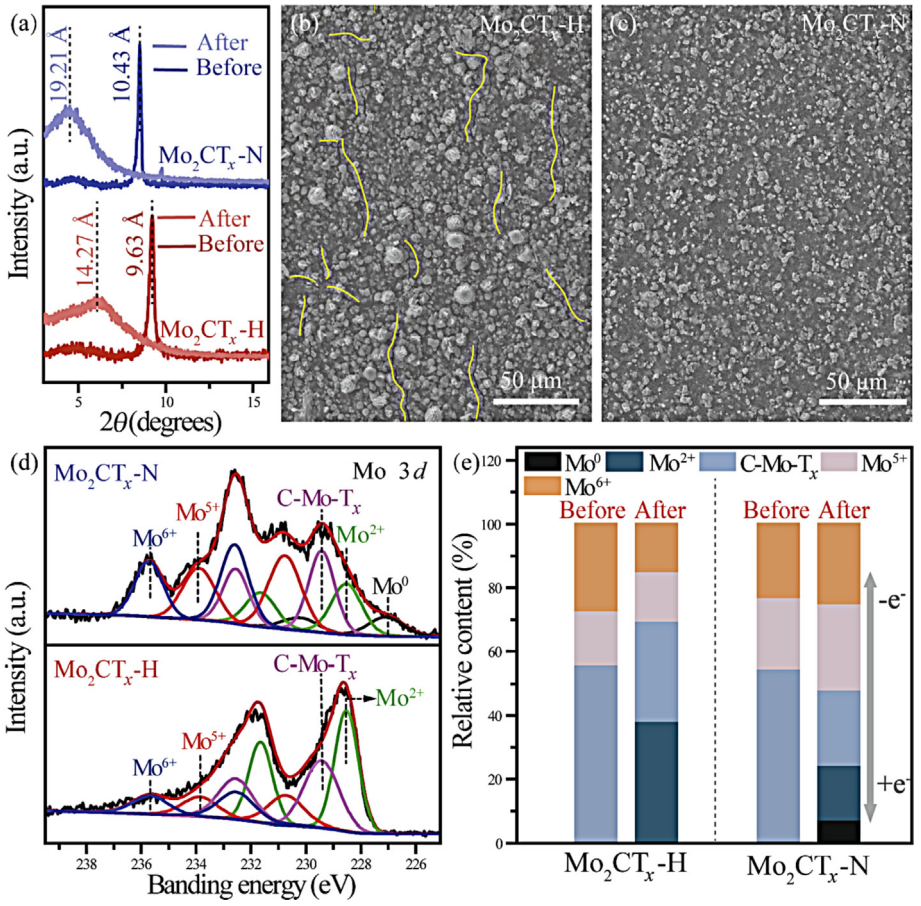

Fig. 4. Stability analysis of Mo_2CT_x-N. (a) XRD patterns of Mo_2CT_x-H and Mo_2CT_x-N before and after 100 cycles. SEM images of (b) Mo_2CT_x-H and (c) Mo_2CT_x-N electrode after 100 cycles. (d) High-resolution Mo 3*d* spectra. (e) The corresponding percentages of Mo-C, Mo^0, Mo^{2+}, C-Mo-T_x, Mo^{5+}, Mo^{6+} in Mo_2CT_x-H and Mo_2CT_x-N.

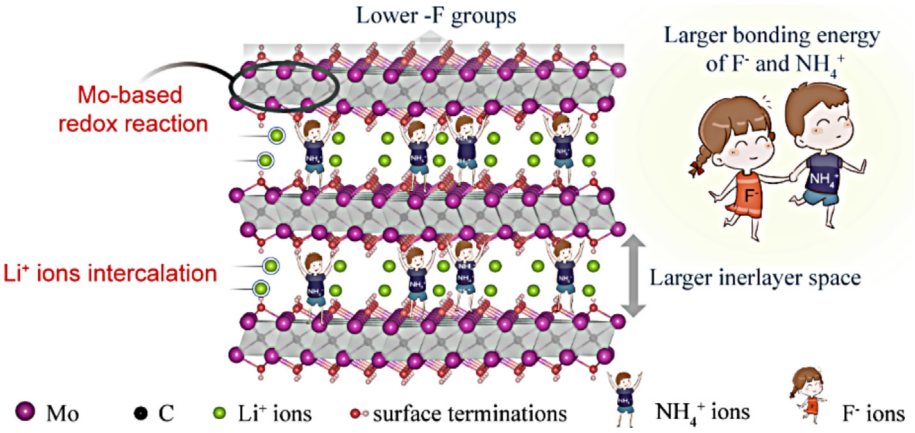

Fig. 5. Schematic view of the Mo_2CT_x-N MXene towards ions storage.

NH_4^+ confined by the adjacent layers of Mo_2CT_x-N MXene, which occupies the electrochemically active sites for Li^+ adsorption. However, the Mo_2CT_x-N contributes to a larger specific capacity in the subsequent cycles. Therefore, the Mo_2CT_x-N electrode exhibited improved cycling stability with a higher capacity retention of 54.97% than Mo_2CT_x-H (39.17%) from the 5th to 100th cycle, which originated from the pillaring effect of the NH_4^+ ions between MXene layers and the more ordered structure [36]. The Mo_2CT_x-N delivered an improved reversible capacity of 384.6 mAh g^{-1} at 200 mA g^{-1} after 100 cycles. With the increase of current densities from 0.1, 0.2, 0.5, 1, 2 to 5C (1C = 500 mA g^{-1}), the discharge capacities of Mo_2CT_x-N varied from 559, 444, 313.2, 199.3, 112.5 to 56.9 mAh g^{-1}. When the current density returns to 0.1C, a reversible capacity of 497.5 mAh g^{-1}can be restored. Furthermore, a comparison of the Li storage-capability of Mo_2CT_x-N with a series of reported MXenes is shown in Fig. 3(e) [36,46,58–61].

3.3. Microstructural evolution and energy storage mechanism of Mo_2CT_x upon cycles

In order to further explore the structural change upon cycles, the electrodes after 100 cycles were investigated. Fig. 4(a) shows the interlayer spacing of Mo_2CT_x-H and Mo_2CT_x-N after cycling is larger than that before cycling. The expansion of the interlayer spacing of Mo_2CT_x-N (8.78 Å) after cycling is larger than that of Mo_2CT_x-H (4.64 Å). This can be ascribed to the intercalation of more Li^+ between the Mo_2CT_x-N layers during the cycling process. Compared to Mo_2CT_x-H, the Mo_2CT_x-N achieves less FWHM after cycles, indicating an improved order degree. Thus, the improved structural stability is induced for the migration of electrolyte ions.

SEM images of Mo_2CT_x-H and Mo_2CT_x-N electrodes after 100 cycles are shown in Fig. 4(b and c) and Fig. S13 and S14. More cracks appear on the Mo_2CT_x-H electrode after 100 cycles (yellow curves highlighted), indicating a smaller interlayer spacing and higher electrochemically activity in the initial cycles lead to larger stress during lithiation/delithiation.

To shed light on the mechanism in the electrochemical performance, *ex situ* XPS (Fig. S15) was employed to survey the changed valence states of Mo of Mo_2CT_x-N during the charge (discharge) processes. The Mo 3*d* peaks shift to higher (lower) binding energies, implying that the valence states of Mo increase (decrease) during the charge (discharge) process. It indicates the evolution of the valence behavior of Mo upon the cyclic process. Besides, XPS was conducted after 100 cycles (Fig. 4d). The C-Mo-T_x species of Mo_2CT_x-N reduces more than that of Mo_2CT_x-H (Fig. 4d and e and Fig. S16), indicating more Mo of Mo_2CT_x-N participates in the reversible redox reaction upon the cyclic process due to the lower -F content. The XPS survey spectra and high-resolution spectra C 1 *s*, F 1 *s*, O 1 *s* of Mo_2CT_x-H and Mo_2CT_x-N after 100 cycles are shown in Fig. S17. Moreover, the electrochemical testing after 100 cycles is shown in Fig. S18. The Mo_2CT_x-N delivered an improved capacitance than Mo_2CT_x-H after 100 cycles. Based on the aforementioned analysis, a schematic illustration (Fig. 5) presents the Mo_2CT_x-N MXene's features for ionic storage.

4. Conclusions

NH_4^+ ions pre-intercalated Mo_2CT_x MXene was obtained via a one-step hydrothermal method with NH_4F solvent. The pre-intercalated NH_4^+ ions cannot only pillar the adjacent MXene layers by spatial occupation but also tune the arrangement more orderly. As a result, a larger distance and spacing of the interlayers were achieved. Besides, the higher binding energy of F^- and NH_4^+ induced a lower content of -F in Mo_2CT_x-N MXene. More Mo of Mo_2CT_x-N underwent a valence evolution in the reversible redox reactions due to the direct exposure to Li^+. As a result, the Mo_2CT_x-N delivered an improved electrochemical storage capability. Thus, through pinpointing Li^+ storage mechanism of NH_4^+ pre-intercalated Mo_2CT_x MXene, our findings lay a foundation for architecting the chemistry of the MXene layers and between them, and offer a guideline for utilizing non-metallic ions pre-intercalated layered materials to tune the interlayer environments for optimal packaged performance.

Declaration of competing interest

The authors declare that they have no known competing financial interests or personal relationships that could have appeared to influence the work reported in this paper.

Acknowledgments

Supported by the National Natural Science Foundation of China (51932003, 51872115), 2020 International Cooperation Project of the Department of Science and Technology of Jilin Province (20200801001GH), the Science and Technology Research Project of Education Department of Jilin Province (JJKH20210453KJ, JJKH20210449KJ), and the Joint Research Fund of Key Laboratory of Functional Materials Physics and Chemistry (Jilin Normal University) Ministry of Education (202101).

Appendix A. Supplementary data

Supplementary data to this article can be found online at https://doi.org/10.1016/j.jechem.2022.04.030.

References

[1] H. Cheng, J.G. Shapter, Y.Y. Li, G. Gao, J. Energy Chem. 57 (2021) 451–468.
[2] F. Xiao, X.H. Chen, J.K. Zhang, C.M. Huang, T. Hu, B. Hong, J.T. Xu, J. Energy Chem. 48 (2020) 122–127.
[3] Y. Wang, L. Zhang, F. Zhang, X. Ding, K. Shin, Y. Tang, J. Energy Chem. 58 (2021) 602–609.
[4] M. Lu, B.S. Zhang, W. Zhang, W.T. Zheng, J. Energy Chem. 41 (2020) 1–2.
[5] X. Tang, X. Guo, W. Wu, G. Wang, Adv. Energy Mater. 8 (2018) 1801897.
[6] J. Luo, C. Fang, C. Jin, H. Yuan, O. Sheng, R. Fang, W. Zhang, H. Huang, Y. Gan, Y. Xia, C. Liang, J. Zhang, W. Li, X. Tao, J. Mater. Chem. A. 6 (2018) 7794–7806.
[7] J. Ma, S. Zheng, Y. Cao, Y. Zhu, P. Das, H. Wang, Y. Liu, J. Wang, L. Chi, S. Liu, Z.-S. Wu, Adv. Energy Mater. 11 (2021) 2100746.
[8] S. Kajiyama, L. Szabova, K. Sodeyama, H. Iinuma, R. Morita, K. Gotoh, Y. Tateyama, M. Okubo, A. Yamada, ACS Nano 10 (2016) 3334–3341.
[9] X. Wang, X. Shen, Y. Gao, Z. Wang, R. Yu, L. Chen, J. Am. Chem. Soc. 137 (2015) 2715–2721.
[10] M.R. Lukatskaya, O. Mashtalir, C.E. Ren, Y. Dall'Agnese, P. Rozier, P.L. Taberna, M. Naguib, P. Simon, M.W. Barsoum, Y. Gogotsi, Science 341 (2013) 1502–1505.
[11] S. Guo, Q. Zhang, Adv. Energy Mater. 10 (2020) 2000484.
[12] M. Sheng, F. Zhang, B. Ji, X. Tong, Y. Tang, Adv. Energy Mater. 7 (2017) 1601963.
[13] H. Wang, C. Wang, Y. Tang, EcoMat 3 (2021) e12172.
[14] C. Eames, M.S. Islam, J. Am. Chem. Soc. 136 (2014) 16270–16276.
[15] J. Li, X. Yuan, C. Lin, Y. Yang, L. Xu, X. Du, J. Xie, J. Lin, J. Sun, Adv. Energy Mater. 7 (2017) 1602725.
[16] M. Lu, W.J. Han, H.J. Li, H.B. Li, B.S. Zhang, W. Zhang, W.T. Zheng, Adv. Mater. Interfaces 6 (2019) 1900160.
[17] W. Zhang, D. Wang, W. Zheng, J. Energy Chem. 41 (2020) 100–106.
[18] J. Pang, R.G. Mendes, A. Bachmatiuk, L. Zhao, H.Q. Ta, T. Gemming, H. Liu, Z. Liu, M.H. Rummeli, Chem. Soc. Rev. 48 (2019) 72–133.
[19] H. Xu, Q. Yan, W. Yao, C.-S. Lee, Y. Tang, Small Struct. (2022) 2100217. (in press) https://doi.org/10.1002/sstr.202100217.
[20] X.W. Ou, D.C. Gong, C.J. Han, Z. Liu, Y.B. Tang, Adv. Energy Mater. 11 (2021) 2102498.
[21] Z.W. Seh, K.D. Fredrickson, B. Anasori, J. Kibsgaard, A.L. Strickler, M.R. Lukatskaya, Y. Gogotsi, T.F. Jaramillo, A. Vojvodic, ACS Energy Lett. 1 (2016) 589–594.
[22] M. Lu, H. Li, W. Han, J. Chen, W. Shi, J. Wang, X.-M. Meng, J. Qi, H. Li, B. Zhang, W. Zhang, W. Zheng, J. Energy Chem. 31 (2019) 148–153.
[23] V. Mehta, H.S. Saini, S. Srivastava, M.K. Kashyap, K. Tankeshwar, J. Phys. Chem. C. 123 (2019) 25052–25060.
[24] X. Shi, W. Zhang, J. Wang, W. Zheng, K. Huang, H. Zhang, S. Feng, H. Chen, Adv. Energy Mater. 6 (2016) 1601378.
[25] Q. Gu, M. Lu, J. Chen, Y. Qi, B. Zhang, Particuology 57 (2021) 139–145.
[26] X. Li, M. Li, Q. Yang, D. Wang, L. Ma, G. Liang, Z. Huang, B. Dong, Q. Huang, C. Zhi, Adv. Energy Mater. 10 (2020) 2001394.
[27] Y. Wang, M. Liu, Z. Wang, Q. Gu, B. Liu, C. Zhao, J. Zhang, S. Xu, M. Lu, H. Li, B. Zhang, J. Energy Chem. 68 (2022) 306–313.
[28] D. Kim, T.Y. Ko, H. Kim, G.H. Lee, S. Cho, C.M. Koo, ACS Nano 13 (2019) 13818–13828.
[29] B. Ahmed, D.H. Anjum, Y. Gogotsi, H.N. Alshareef, Nano Energy 34 (2017) 249–256.
[30] M. Xu, L. Liang, J. Qi, T. Wu, D. Zhou, Z. Xiao, Small 17 (2021) 2007446.
[31] Z. Xia, X. Chen, H. Ci, Z. Fan, Y. Yi, W. Yin, N. Wei, J. Cai, Y. Zhang, J. Sun, J. Energy Chem. 53 (2021) 155–162.
[32] M. Lu, W. Han, H. Li, W. Zhang, B. Zhang, J. Energy Chem. 48 (2020) 344–363.
[33] F. Liu, A. Zhou, J. Chen, J. Jin, W. Zhou, L. Wang, Q. Hu, Appl. Surf. Sci. 416 (2017) 781–789.
[34] H. Kim, B. Anasori, Y. Gogotsi, H.N. Alshareef, Chem. Maters. 29 (2017) 6472–6479.
[35] Y. Guo, S. Jin, L. Wang, P. He, Q. Hu, L.-Z. Fan, A. Zhou, Ceram. Int. 46 (2020) 19550–19556.
[36] M. Lu, Y. Zhang, J. Chen, W. Han, W. Zhang, H. Li, X. Zhang, B. Zhang, J. Energy Chem. 49 (2020) 358–364.
[37] W. Han, M. Lu, J. Chen, H. Li, H. Li, B. Zhang, W. Zhang, W. Zheng, J. Mater. Chem. A. 8 (2020) 16265–16270.
[38] O. Chaix-Pluchery, A. Thore, S. Kota, J. Halim, C. Hu, J. Rosen, T. Ouisse, M.W. Barsoum, J. Raman Spectrosc. 48 (2017) 631–638.
[39] Y. Feng, K. Song, W. Zhang, X. Zhou, S.J. Yoo, J.-G. Kim, S. Qiao, Y. Qi, X. Zou, Z. Chen, T. Qin, N. Yue, Z. Wang, D. Li, W. Zheng, J. Energy Chem. 70 (2022) 211–218.
[40] J. Wang, Y.J. Hu, B.F. Yang, X. Wang, J.W. Qin, M.H. Cao, Nano Energy 87 (2021) 106053.
[41] M. Ekimova, W. Quevedo, L. Szyc, M. Iannuzzi, P. Wernet, M. Odelius, E.T.J. Nibbering, J. Am. Chem. Soc. 139 (2017) 12773–12783.
[42] E. Lee, A. VahidMohammadi, B.C. Prorok, Y.S. Yoon, M. Beidaghi, D.-J. Kim, A.C. S. Appl. Mater. Interfaces 9 (2017) 37184–37190.
[43] P. Yan, R. Zhang, J. Jia, C. Wu, A. Zhou, J. Xu, X. Zhang, J. Power Sources 284 (2015) 38–43.
[44] U. Qumar, J. Hassan, S. Naz, A. Haider, A. Raza, A. Ul-Hamid, J. Haider, I. Shahzadi, I. Ahmad, M. Ikram, Nanotechnology. 32 (2021) 255704.
[45] C.C. Lai, R. Meshkian, M. Dahlqvist, J. Lu, L.Å. Näslund, O. Rivin, E.N. Caspi, O. Ozeri, L. Hultman, P. Eklund, M.W. Barsoum, J. Rosen, Acta Mater. 99 (2015) 157–164.
[46] J. Mei, G.A. Ayoko, C. Hu, J.M. Bell, Z. Sun, SM&T 25 (2020) e00156.
[47] J. Halim, S. Kota, M.R. Lukatskaya, M. Naguib, M.-Q. Zhao, E.J. Moon, J. Pitock, J. Nanda, S.J. May, Y. Gogotsi, M.W. Barsoum, Adv. Funct. Mater. 26 (2016) 3118–3127.
[48] J. Halim, K.M. Cook, M. Naguib, P. Eklund, Y. Gogotsi, J. Rosen, M.W. Barsoum, Appl. Surf. Sci. 362 (2016) 406–417.
[49] T.T. Qin, X.F. Chu, T. Deng, B.R. Wang, X.Y. Zhang, T.W. Dong, Z.M. Li, X.F. Fan, X. Ge, Z.Z. Wang, P. Wang, W. Zhang, W.T. Zheng, J. Energy Chem. 48 (2020) 21–28.
[50] H. Zhang, Q. Qi, P. Zhang, W. Zheng, J. Chen, A. Zhou, W. Tian, W. Zhang, Z. Sun, A.C.S. Appl. Energy Mater. 2 (2019) 705–714.
[51] M. Lu, W. Han, H. Li, W. Shi, J. Wang, B. Zhang, Y. Zhou, H. Li, W. Zhang, W. Zheng, Energy Stor. Mater. 16 (2019) 163–168.
[52] X. Zheng, J. Shen, Q. Hu, W. Nie, Z. Wang, L. Zou, C. Li, Nanoscale 13 (2021) 1832–1841.
[53] Y. Zheng, T. Deng, W. Zhang, W. Zheng, J. Energy Chem. 47 (2020) 210–216.
[54] He Yang, Tingting Qin, Xinyan Zhou, Yu Feng, Zizhun Wang, Xin Ge, Nailin Yue, Dabing LI, Wei Zhang, Weitao Zheng, Boosting the kinetics of PF_6^- into graphitic layers for the optimal cathode of dual-ion batteries: the rehearsal of pre-intercalating Li^+, Journal of Energy Chemistry 71 (2022) 392–399, https://doi.org/10.1016/j.jechem.2022.04.009.
[55] Z. Pan, T. Qin, W. Zhang, X. Chu, T. Dong, N. Yue, Z. Wang, W. Zheng, J. Energy Chem. 68 (2022) 42–48.
[56] Q. Gu, Y. Qi, W. Hua, T. Shang, J. Chen, L. Jiang, L. Li, M. Lu, Y. Zhang, X. Liu, Y. Wan, B. Zhang, J. Energy Chem. 69 (2022) 490–496.
[57] X.Y. Shi, S.S. Yu, T. Deng, W. Zhang, W.T. Zheng, J. Energy Chem. 44 (2020) 13–18.
[58] J. Luo, W. Zhang, H. Yuan, C. Jin, L. Zhang, H. Huang, C. Liang, Y. Xia, J. Zhang, Y. Gan, X. Tao, ACS Nano 11 (2017) 2459–2469.
[59] J. Zhou, S. Lin, Y. Huang, P. Tong, B. Zhao, X. Zhu, Y. Sun, Chem. Eng. J. 373 (2019) 203–212.
[60] B. Ahmed, D.H. Anjum, M.N. Hedhili, Y. Gogotsi, H.N. Alshareef, Nanoscale 8 (2016) 7580–7587.
[61] R. Liu, W. Cao, D. Han, Y. Mo, H. Zeng, H. Yang, W. Li, J. Alloys Compd. 793 (2019) 505–511.